INTERNATIONAL JOURNAL FOR NUMERICAL METHODS IN FLUIDS, VOL. 16, 1051–1078 (1993)

DIRECT SIMULATION OF TURBULENT FLOW AND HEAT TRANSFER IN A CHANNEL. PART I: SMOOTH WALLS

JEFFREY RUTLEDGE

Thinking Machines Corporation, 12 Greenway Plaza, Houston, TX 77046, U.S.A.

AND

CHARLES A. SLEICHER

Department of Chemical Engineering, University of Washington, Seattle, WA 98195, U.S.A.

SUMMARY

Interest in the use of supercomputers for the direct numerical calculation of turbulence prompts the development of efficient numerical techniques so that calculation at higher Reynolds numbers might be made. This paper presents an efficient pseudo-spectral technique, similar to but different from others that have recently appeared, for the calculation of momentum and heat transfer to a constant-property, turbulent fluid in a two-dimensional channel with walls at different, uniform temperature. The code uses no empiricism, although periodic boundary conditions are used for fluctuating quantities in the streamwise and spanwise directions.

Calculations were made for a Prandtl number of 0·72 and Reynolds number based on friction velocity and channel half-height of 180 or 2800 based on channel half-height and average velocity. Calculations of mean velocity profile, turbulence intensities, skewness, flatness, Reynolds stress and eddy diffusivity of heat near a wall compare favourably with experimental results. Representative contour plots of the temperature field near the wall and of the spanwise and streamwise two-point velocity correlations are given.

Deficiencies are that the calculation requires many hours on a fast computer with a large high-speed memory and that the grid size in each direction for appropriate resolution is approximately proportional to the square of the Reynolds number and to the Prandtl number raised to some power greater than one.

KEY WORDS Numerical simulation Turbulence Heat transfer

1. INTRODUCTION

As part of a project to investigate the effect of wall roughness on heat transfer, we developed a Navier–Stokes equation solver to calculate the velocity field for the problem of heat transfer through a turbulent fluid in a rectangular channel. Others have developed similar codes, but ours is quite efficient and contains some differences that may be useful. In the past 20 years much research has been done on the use of 'models' of turbulence to calculate turbulent flow patterns in a variety of geometries. These models have been developed as a means of solving the closure problem—the generation of moments of higher order upon averaging the transport equation for any given moment. The most well known of these models is the k–ε model, which contains transport equations for k, the local turbulent kinetic energy, and ε, the local mean rate of energy dissipation. Reynolds stress models are much more complicated but give superior results and have recently received more attention than k-ε models. The models do not avoid empiricism, for

0271–2091/93/121051–28$19.00

Received 8 September 1992
Revised 28 December 1992

a number of constants and functions must be specified or modelled. The primary advantage of these models is that they can sometimes be extrapolated from one geometry to another, whereas mixing-length and eddy-viscosity models are useful only when the eddy viscosity has been empirically determined in a similar geometry. Ferziger[1] has cautioned against reliance on the k–ε model in some cases, and it is known that the model does not work well near solid boundaries. Moreover the closure empiricisms in these models are based on smooth boundary experimental data, and we wish to investigate the effect of a pattern of roughness on the wall.

An alternative to the analysis of turbulence by modelling the terms in the higher-order transport equations is direct simulation. In this method empiricism is avoided and all three components of the complete, time-dependent Navier–Stokes equations are solved numerically in a three-dimensional grid in space. The vast amount of data so generated can then be averaged as desired to obtain quantities such as the profiles of average velocity, temperature, pressure and stress. The disadvantage, of course, is the enormous computational resources required and the difficulty, often, in obtaining numerical stability and convergence. To obtain satisfactory results at reduced computational effort has been the subject of many papers, and a few of them are referred to here.

The tool that makes direct numerical calculation of turbulence feasible is spectral analysis. It was apparently Orszag and Peterson[2] who first introduced the idea of applying the spectral method for solving problems of turbulence, a suggestion that met with much skepticism at the time. The spectral method involves approximating a function with a series that is required to satisfy the differential equation exactly at specified collocation points, and it can sometimes require an order of magnitude less computer time and storage than finite difference methods. Much of the speed of the method is due to the use of fast Fourier transforms.

The application of spectral methods to wall-bounded turbulence apparently began in 1980 with the paper by Orszag and Kells[3] on transition to turbulence in Poiseuille and plane Couette flow. Application of spectral techniques to fully developed channel flow has been reported by Moin and Kim,[4,5] Moser and Moin[6] and Kim *et al.*[7] A little later, Lyons *et al.*[8,9] published two papers on essentially the same problem as the one studied in the present paper. The principal differences are the Reynolds number (300 vs. our 360), the Prandtl number (1·0 vs our 0·72), the size of the grid (up to $128 \times 128 \times 65$ vs. our $144 \times 144 \times 65$), significant differences in the computational algorithms, and differences in what quantities were calculated. The principal results, however, are in quite close agreement.

The starting point for all of the foregoing studies is the incompressible Navier–Stokes equation. Orszag[10] has shown that the usual Eulerian form of the Navier–Stokes equation does not conserve kinetic energy when spectral representations are used. However, by use of a vector identity, the Navier–Stokes equations can be converted into the following form, which conserves energy to machine precision for most types of discretization of differential operators:[1]

$$\frac{\partial u}{\partial t} = u \times \omega - \nabla \pi + \frac{1}{Re} \nabla^2 u + F, \tag{1}$$

where

$$\omega = \nabla \times u,$$

$$\pi = p + \frac{u \cdot u}{2},$$

F = external body forces.

This form of the Navier–Stokes equation was also used in the previous investigations.

The time-stepping algorithm

Since the equations to be solved are time-dependent, some efficient technique must be used for advancing the velocity field in time. The algorithm used here and by most other investigators is mainly due to Chorin.[11] A good summary of the technique has been given by Leonard and Wray.[12] The method involves defining a set of intermediate, non-physical variables that permit breaking each time step into a set of four intermediate, fractional steps. The intermediate variables are only temporarily stored and are used only to get the next step in the velocity field. In order to complete a time step, each of the fractional steps must be solved in sequential order, and two of those steps require integrating differential equations. This has lead to a controversy on how to handle the boundary conditions on one of the equations, the equation for the pressure, which contains one of the intermediate variables. Some authors used actual boundary conditions on the intermediate variables, but Kim and Moin[13] realized, perhaps before anyone else, that using actual boundary conditions on the intermediate, non-physical variables creates problems, and they recommended resolving the problem with a technique that uses a staggered grid for the pressure. However, Abdallah[14] has shown that the use of staggered grids for the pressure field violates a compatibility condition (Green's theorem) that stems from the derivation of the equation for the pressure.

Two other methods for attacking the pressure equation are evidently correct, though each leads to some increased computational effort. The first was first published by Ku *et al.*[15] and a similar technique was used by Lyons *et al.*[8,9] In this method the boundary condition on the pressure equation, or second step, comes from applying the Navier–Stokes and continuity equations at the boundary. Unfortunately, the results from the fourth step are required to calculate boundary condition on the pressure step, and this coupling destroys the sequential nature of the splitting method. However, since coupling is only through the boundary conditions and not through the whole field, a small Green's function or influence matrix can be precalculated once for all time to determine the influence of the boundary conditions. With this matrix and making an extra pass through the last three steps in the splitting method, a nearly non-divergent velocity field can be calculated at each time step with but little extra computational effort.

The second method to attack the pressure boundary condition problem, and the one used here, is to eliminate the pressure from the Navier–Stokes equations. An example of this technique has been given by Kim *et al.*[7]

2. ANALYSIS

The governing equations for our problem are the incompressible Navier–Stokes equation (1), and temperature equation

$$\frac{\partial T}{\partial t}+u\cdot\nabla T=\frac{1}{Pe}\nabla^2 T, \tag{2}$$

where

$$Pe=Pr\ Re.$$

The external pressure gradient is taken to be constant and viscous dissipation is neglected. All physical properties are taken to be independent of temperature so that the velocity field can be calculated independently of the temperature field, i.e. the temperature is a passive scalar. The length scale for (1) and (2) is the half-height between the parallel plates, δ. The velocity scale is the friction velocity, u_τ, which is defined as $(\tau_w/\rho)^{1/2}$ where τ_w is the mean shear at the wall and ρ is the

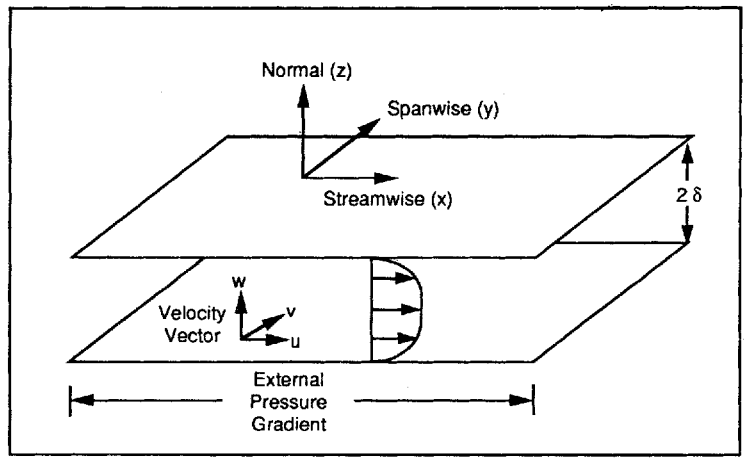

Figure 1. Geometry and nomenclature

density. It is easily shown that the external pressure drop is related to τ_w so that $F=1$ in (1). The time scale is the length scale divided by the velocity scale. The temperature is non-dimensionalized so that temperatures on the upper and lower boundaries are constant at 1 and -1. With the given scaling the Reynolds number is $u_\tau\delta/\nu$, where ν is kinematic viscosity. The Prandtl number is α/ν, where α thermal diffusivity.

These equations are applied to the simulation domain shown in Figure 1, which shows the nomenclature. Streamwise refers to the direction aligned with the pressure gradient, normal is the direction perpendicular to the walls, and spanwise is the direction parallel to the boundaries and perpendicular to the pressure gradient. These equations are the same as those used by Lyons *et al.* except that the symbols for the normal and spanwise directions are interchanged.

Before (1) is discretized, it is cast in the form used by Kim *et al.*[7] to eliminate the pressure. A derivation of the transformation has been given by Rutledge[16]

$$\frac{\partial}{\partial t}\nabla^2 w=\frac{1}{Re}\nabla^4 w+h_3, \quad \text{with } w,\ \frac{\partial w}{\partial z} \text{ on } \partial D, \tag{3}$$

where

$$h_3=-\frac{\partial}{\partial z}\left(\frac{\partial H_1}{\partial x}+\frac{\partial H_2}{\partial y}\right)+\left(\frac{\partial^2}{\partial x^2}+\frac{\partial^2}{\partial y^2}\right)H_3,$$

$$\frac{\partial}{\partial t}g=\frac{1}{Re}\nabla^2 g+h_g, \quad \text{with } g \text{ on } \partial D, \tag{4}$$

where

$$h_g=\frac{\partial H_1}{\partial y}-\frac{\partial H_2}{\partial x},$$

$$H_i=(u\times\nabla\times u)_i+F_i \quad (F_i=\text{external forces}),$$

$$g=\frac{\partial u}{\partial y}-\frac{\partial v}{\partial x},$$

$$f+\frac{\partial w}{\partial z}=0, \tag{5}$$

$$f=\frac{\partial u}{\partial x}+\frac{\partial v}{\partial y}, \tag{6}$$

$$g=\frac{\partial u}{\partial y}-\frac{\partial v}{\partial x}. \tag{7}$$

The symbol ∂D refers to a boundary condition and means on the border of the domain (the two planes). Note that g is the normal component of vorticity and f is a new variable introduced by splitting the equation of continuity into two parts. A disadvantage of this form is the required integration of the biharmonic operator in (3). To avoid dealing directly with it, we introduce a new intermediate variable, ϕ, and split the equation into two parts:

$$\frac{\partial \phi}{\partial t}=\frac{1}{Re}\nabla^2\phi+h_3, \quad \text{with } \phi \text{ chosen on } \partial D \text{ so that } \quad \frac{\partial u}{\partial x}+\frac{\partial v}{\partial y}+\frac{\partial w}{\partial z}=0 \text{ on } \partial D. \tag{8}$$

where

$$\nabla^2 w=\phi, \quad \text{with } w \text{ on } \partial D.$$

Discretization in time

Equations (4) and (8) are now discretized in time by splitting them so that the non-linear terms are treated explicitly with a Runge–Kutta technique whereas the linear (or viscous) parts of the equations, which are operated on by the Laplacian operator, are treated implicitly with a Crank–Nicolson technique. These time-split equations are

$$\frac{\phi^n-\phi^{n-1}}{\Delta t}=\alpha h_3^n+\beta h_3^{n-1}+\frac{\nabla^2}{Re}\left(\frac{\phi^{n+1}+\phi^n}{2}\right), \tag{9}$$

$$\frac{g^{n+1}-g^n}{\Delta t}=\alpha h_g^n+\beta h_g^{n-1}+\frac{\nabla^2}{Re}\left(\frac{g^n+g^{n+1}}{2}\right). \tag{10}$$

The non-linear (or convective) parts, h_g and h_3, are treated explicitly by choosing the appropriate weighting α and β. Since the non-linear parts are treated explicitly, the step size, Δt, must be set below a certain limit to avoid numerical instability. Most investigators choose $\alpha=3/2$ and $\beta=1/2$, which is an Adams–Bashforth treatment. There is no known explicit method for applying this treatment to the convective diffusion equation that is stable when the Courant number,

$$C_N=\pi\Delta t\left(\left|\frac{u}{\Delta x}\right|_{\max}+\left|\frac{v}{\Delta y}\right|_{\max}+\left|\frac{w}{\Delta z}\right|_{\max}\right), \tag{11}$$

is greater than one, and it is usually assumed that $C_N<1$ is a necessary condition for stability. $C_N<1$, however, is not in general a sufficient condition for stability.

A more elaborate scheme for choosing α and β was suggested by Wray and Hussaini.[17] It involves breaking the time step into a set of fractional steps and cycling through a set of different fractions of the step size and of α and β so that the non-linear part is integrated in the Runge–Kutta sense. Moreover, for the first set in the cycle, β can be forced to zero so only the solution at the nth time step is required to start the model. This gives one the freedom to adjust Δt each time the cycling reaches the first set of the cycle. Thus, the time step can be maximized to track the Courant number so that it can be kept just under its critical value. A good example of

Table I. Runge–Kutta–Wray integration constants

Fractional step	γ	α	β
Step 1	8/15	1	0
Step 2	2/15	25/8	−17/8
Step 3	1/3	9/4	5/4

The fractional step size is $\gamma\,\Delta t$, where Δt is the total step size

the technique is given by Spalart.[18] His choice of the fractional step sizes and weighting constants are given in Table I. The Runge–Kutta scheme is applied by cycling through a set of three different values of Δt, α and β shown in Table I.

Spalart[18] chose β to be zero on the first step so the scheme is 'self-starting', and only one solution is required to start the time stepping. The constants were also chosen to give third-order accuracy in the non-linear part. (The Crank–Nicolson treatment gives second-order accuracy for the linear part of (4); so, third-order accuracy is over-kill.) This scheme gives a critical Courant number equal to the square root of 3. Thus, this scheme will be stable for a step size about 1·7 larger than the maximum in the Adams–Bashforth method but a cost of 3 times more computational work. The appeal of the method, however, is the ease with which the step size can be changed. In Spalart's scheme the step size can be set so that the Courant number is always nearly critical.

Equations (9) and (10) are now simplified by grouping all of the $n+1$ terms on the left-hand side and all other terms on the right-hand side:

$$\left(1-\frac{\Delta t}{2Re}\nabla^2\right)g^{n+1}=g_{\mathrm{RHS}}, \tag{12}$$

where

$$g_{\mathrm{RHS}}=\left(1+\frac{\Delta t}{2Re}\nabla^2\right)g^n+\Delta t(\alpha h_g^n+\beta h_g^{n-1})$$

$$\left(1-\frac{\Delta t}{2Re}\nabla^2\right)\phi^{n+1}=\phi_{\mathrm{RHS}}, \tag{13}$$

where

$$\phi_{\mathrm{RHS}}=\left(1+\frac{\Delta t}{2Re}\nabla^2\right)\phi^n+\Delta t(\alpha h_3^n+\beta h_3^{n-1}).$$

Spatial discretization in the streamwise and spanwise directions

Since the turbulence is homogeneous in the streamwise and spanwise directions, the velocity components in those directions can be represented by Fourier series with periodic boundary conditions. Lyons *et al.*[8] have pointed out that this assumption is valid as long as the domain of periodicity is large enough so that all two-point correlation functions become negligibly small within the domain. The periodic solution also relieves us of the problem of solving the inflow–outflow mass balance required in the streamwise direction.

Equations (5)–(7), (12) and (13) are next transformed with respect to the homogeneous directions (x and y) according to the following definition of the discrete Fourier transform, DFT:

$$u(k_1\, k_2, z) = \sum_{i_1=0}^{N_1-1} \sum_{i_2=0}^{N_2-1} u(i_1, i_2, z) \exp\left[2\pi i \left(\frac{i_1 k_1}{\alpha_1 N_1} + \frac{i_2 k_2}{\alpha_2 N_2} \right) \right], \tag{14}$$

where k_1 and k_2 are multiplied by α_1 and α_2 when they do not appear as indicies.

The streamwise and spanwise aspect ratios, α_1 and α_2, are embedded in the wave numbers k_1 and k_2 so that (5)–(7), (12) and (13) become

$$\frac{\mathrm{d}^2}{\mathrm{d}z^2} g^{n+1} - \left(\frac{1}{f_c} + k_1^2 + k_2^2 \right) g^{n+1} = -\frac{1}{f_c} g_{\mathrm{RHS}}, \quad \text{with } g^{n+1} \text{ on } \partial D_z, \tag{15}$$

where

$$f_c = \frac{\Delta t}{2Re},$$

$$\frac{d^2}{\mathrm{d}z^2} \phi^{n+1} - \left(\frac{1}{f_c} + k_1^2 + k_2^2 \right) \phi^{n+1} = -\frac{1}{f_c} \phi_{\mathrm{RHS}}, \quad \text{with } \phi^{n+1} \text{ on } \partial D_z, \tag{16}$$

$$\frac{\mathrm{d}^2}{\mathrm{d}z^2} w^{n+1} - (k_1^2 + k_2^2) w^{n+1} = \phi^{n+1}, \quad \text{with } w^{n+1} \text{ on } \partial D_z, \tag{17}$$

$$f^{n+1} = \frac{\mathrm{d}w^{n+1}}{\mathrm{d}z}, \tag{18}$$

$$f^{n+1} = \mathrm{i}k_1 u^{n+1} + \mathrm{i}k_2 v^{n+1}, \tag{19}$$

$$g^{n+1} = \mathrm{i}k_2 u^{n+1} - \mathrm{i}k_1 v^{n+1}. \tag{20}$$

Since the aspect ratio is embedded into the wave numbers, they are not necessarily integers. Note also that we have not changed the symbols but that all of the variables have been transformed and the independent variables have been changed from (x, y, z) to (k_1, k_2, z).

Fast Fourier Transform (FFT) codes can be used to evaluate the DFTs, and they require $N \log_q(N)$ multiplications to integrate a variable in a given direction of N grid points. The log base, q, is determined by the radix of the DFT, which is usually 2. Using a radix of 2, however, limits the choice of the number of grid points to powers of 2, a severe limitation that affected our choice of the FFT. The FFT we used was written by Temperton[19–21] in Fortran. This FFT is multiradixed and allows N to be composed of factors 2, 3 or 5. It vectorizes perpendicular to the direction being transformed, which means that when the FFT is being performed on the streamwise grid points, the code vectorizes with the spanwise points and *vice versa.*

The variables in (15)–(20) are now complex-valued, which doubles the number of calculations needed to do the DFT integrations. However, since the transformed variables are real-valued, we gain a factor of two because of conjugational symmetry.[22] With this symmetry the span of k_1 and k_2 are $-N_1/2$ to 0 and $-N_2/2$ to $N_2/2-1$, where N_1 and N_2 are the number of grid points in the streamwise and spanwise directions. The result is that the total number of sets of equations to be solved is $N_1 N_2$. Note that the use of Fourier transforms to evaluate derivatives is global or spectral in nature, i.e. when a derivative is taken in a homogeneous direction, the DFT causes every point in that direction to be involved in the evaluation of the derivative.

The right-hand sides of (15) and (16) contain non-linear terms, which become difficult Fourier convolutions in Fourier space. Therefore, as was apparently first done by Fox and Orszag,[23] we

carry out multiplications in real space and differentiations in Fourier space. Everytime a multiplication is to be done, the variables at each grid point are transformed into real space, multiplied, and transformed back into Fourier space to continue the integration. As is now well known, this procedure produces aliasing errors—errors caused by truncation of higher modes that then affect the lower modes. However, Orszag[10] showed that aliasing errors can be eliminated by a simple procedure. Solely for the purpose of evaluating the non-linear terms, zeros are appended to the Fourier series until it has 3/2 more terms . The series is then inverse transformed to a grid in physical space with 3/2 as many points. Multiplication is then done on that physical space mesh and the result transformed back to Fourier space and truncated to the original length. All terms that involve non-linear evaluations were de-aliased.

For each wave-number pair, (15–20) can be solved independently of all other wave-number pairs. It is this wave-number pair decoupling that makes the computations feasible. The order in which (15)–(20) are solved is as follows. First, all right-hand side information (g_{RHS} and ϕ_{RHS}) is evaluated using existing information. The Dirichlet boundary conditions on u^{n+1}, v^{n+1} and w^{n+1} as well as the Neumann condition on w^{n+1} via the continuity equation are known. Next, (15) is solved by using (20) to get the boundary condition. Equations (16) and (17) are solved simultaneously with the aid of a Green's function (discussed later) to set the Dirichlet condition on ϕ^{n+1} so that the Neumann condition on w^{n+1} has the proper value. Then f^{n+1} is evaluated via (18). Lastly, (19) and (20) are used to solve for u^{n+1} and v^{n+1} algebraically through the equations

$$v^{n+1}=\frac{\mathrm{i}k_1 g^{n+1}-\mathrm{i}k_2 f^{n+1}}{k_1^2+k_2^2}, \tag{21}$$

$$u^{n+1}=\frac{-\mathrm{i}k_2 g^{n+1}-\mathrm{i}k_1 f^{n+1}}{k_1^2+k_2^2}. \tag{22}$$

It is easily seen that when the wave-number pair (k_1, k_2) is (0, 0), the solution for u^{n+1} and v^{n+1} is singular and must be treated separately. The equations of motion for this wave-number pair are identical to the equation of motion spatially averaged in the homogeneous directions and then Fourier transformed. Since the external pressure drop is a force appearing as an averaged force, the equations for the (0, 0) mode are the only equations in which it appears. Since the external pressure gradient is the only force keeping the fluid in motion, the solution for this mode feeds energy to all the other modes. From the Fourier-transformed continuity equation and the condition of no mass transport through a solid boundary, it is evident that w^{n+1} for this mode is always zero for all z. We deal with this mode by solving the equations of motion as they are before pressure is eliminated. There is no need to eliminate the dynamic pressure from the (0, 0) mode since the only equation in which it appears has already been solved (the w equation of motion). Thus, the solutions for the u and v velocities for the (0, 0) mode are

$$\frac{\mathrm{d}^2}{\mathrm{d}z^2}u^{n+1}-\frac{1}{f_c}u^{n+1}=-\frac{1}{f_c}u_{\mathrm{RHS}}, \quad \text{with } u^{n+1}=0 \text{ on } \partial D_z, \tag{23}$$

where

$$u_{\mathrm{RHS}}=\left[1+f_c\frac{\mathrm{d}^2}{\mathrm{d}z^2}\right]u^n+\Delta t(\alpha H_1^n+\beta H_1^{n-1}),$$

$$\frac{\mathrm{d}^2}{\mathrm{d}z^2}v^{n+1}-\frac{1}{f_c}v^{n+1}=-\frac{1}{f_c}v_{\mathrm{RHS}}, \quad \text{with } v^{n+1}=0 \text{ on } \partial D_z, \tag{24}$$

where

$$v_{\mathrm{RHS}}=\left[1+f_{\mathrm{c}}\frac{\mathrm{d}^2}{\mathrm{d}z^2}\right]v^n+\Delta t(\alpha H_2^n+\beta H_2^{n-1}).$$

We also give special treatment to any mode that contains the wave numbers $-N_1/2$ or $-N_2/2$ by omitting it from the solution, as is the standard practice, because it is an artefact of the DFT.[22]

Spatial discretization in the normal direction

The use of Fourier series to approximate the velocity distribution in the normal direction is unsatisfactory because of the inability of the expansion to converge uniformly at the channel boundaries (Gibbs phenomenon). Lanczos[24] suggested that a more useful approximation under these circumstances is series of Sturm–Liouville eigenfunctions. Therefore, the normal component of velocity is expanded in a Chebyshev series of the first kind, which is standard for normal integration in our type of problem.[25] Unlike the evenly spaced grid points used in the homogeneous directions, the grid points in the normal direction are more tightly spaced near the boundaries to accomodate the higher gradients there. The positions are obtained from the function $z_j=\cos(j\pi/N_3)$, where j ranges from 0 to N_3. Thus, with 65 points between walls located at -1 and 1, the first point is located at $z=-0{\cdot}00117$ and the central points have an interval of 0·0483.

The use of Chebyshev transforms to integrate the normal direction is basically sound, but in practice two problems arise. The first is in evaluating the second derivative. If we transform a vector of points into Chebyshev coefficient space, use a recurrence scheme to form the Chebyshev transform of the derivative, and then transform back to get the derivative of the vector, the result is satisfactory. If, however, the recurrence relation is applied twice in Chebyshev space, the resulting second derivative has round-off error problems. When implemented into the whole scheme of the solution of the Navier–Stokes equations, this error causes numerical instability. However, we found that simply squaring the first-derivative collocation matrix and using that to take second derivatives yielded no problems. The second problem is in trying to solve the ordinary differential equations (15)–(17) in Chebyshev coefficient space. Apparently, the round-off errors are so severe in evaluating the last coefficients of the series that these coefficients do not contribute to the series correctly. Thus, the only place where we were able to use the fast Chebyshev transform technique is in the evaluation of the first derivative in the normal direction. Therefore, we stayed in real space rather than spectral space when calculating in the normal direction. The normal discretization was done with collocation matrices regardless of whether a Chebyshev recurrence relation or a collocation matrix was used to take a derivative. The next task is to economize the matrix operations needed to discretize (15)–(17).

When collocation of the Chebyshev grid is applied to (15)–(17), they assume the following form:

$$[B_{ij}-cI_{ij}]\,g_j^{n+1}=-\frac{1}{f_{\mathrm{c}}}(g_{\mathrm{RHS}})_i, \tag{25}$$

where

$$c=\left(\frac{1}{f_{\mathrm{c}}}+k_1^2+k_2^2\right),$$

$$i=0 \text{ to } N_3 \quad \text{and} \quad j=0 \text{ to } N_3;$$

$$[B_{ij}-cI_{ij}]\,\phi_j^{n+1}=-\frac{1}{f_{\mathrm{c}}}(\phi_{\mathrm{RHS}})_i, \tag{26}$$

where

$$i=0 \text{ to } N_3 \quad \text{and} \quad j=0 \text{ to } N_3;$$

$$[B_{ij}-c_w I_{ij}]\, w_j^{n+1} = -\frac{1}{f_c}\, \phi_i^{n+1}, \tag{27}$$

where

$$c_w = k_1^2 + k_2^2,$$

$$i=0 \text{ to } N_3 \quad \text{and} \quad j=0 \text{ to } N_3.$$

B_{ij} is the square of the first-derivative collocation matrix (i.e. second-derivative collocation matrix) and I_{ij} is the identity matrix. These equations have not been subject to boundary conditions. To apply them, we bring the outer columns of the collocation matrix multiplied by the variable at the boundaries over to the right-hand side with the rest of the known information. The outer rows of the collocation matrix are then discarded. Thus, equations (25)–(27) take the following form:

$$[B_{ij}-cI_{ij}]\, g_j^{n+1} = -\frac{1}{f_c}\,(g_{\mathrm{RHS}})_i - B_{ik} g_k^{n+1}, \tag{28}$$

where

$$i=1 \text{ to } N_3-1 \quad \text{and} \quad j=1 \text{ to } N_3-1,$$

$$k=0 \text{ and } N_3;$$

$$[B_{ij}-cI_{ij}]\, \phi_j^{n+1} = -\frac{1}{f_c}\,(\phi_{\mathrm{RHS}})_i - B_{ik} \phi_k^{n+1}, \tag{29}$$

where

$$i=1 \text{ to } N_3-1 \quad \text{and} \quad j=1 \text{ to } N_3-1,$$

$$k=0 \text{ and } N_3;$$

$$[B_{ij}-c_w I_{ij}]\, w_j^{n+1} = \phi_i^{n+1} - B_{ik} w_k^{n+1}, \tag{30}$$

where

$$i=1 \text{ to } N_3-1 \quad \text{and} \quad j=1 \text{ to } N_3-1,$$

$$k=0 \text{ and } N_3.$$

Solution of the discretized equations

Since (28)–(30) are unique for each wave-number pair, and c is a function of wave number, there are $N_1 N_2$ sets of N_3 linear systems to solve to get an update on the solution for each time step. Solving the linear systems would take on order $N_1 N_2 N_3 N_3 N_3$ operations for each time step. Since typical grids are of order 100 points in each direction, this procedure would require about 10^{10} operations for each time step, a prohibitive number. An alternative scheme was used by Gottlieb and Orszag[26] for a somewhat different application and will be illustrated by application to (28). It can be shown that the inverse of the matrix of the linear system, equation (28), can be expressed as follows:

$$[B_{ij}-cI_{ij}]^{-1} = e_{jp}\left(\frac{e_{pi}^{-1}}{\lambda_p - c}\right), \tag{31}$$

where

$$e_{jp} = \text{eigenvectors of } B_{ji},$$

$$\lambda_p = \text{eigenvalues of } B_{ji},$$

$$i, j, p = 1 \text{ to } N_3 - 1.$$

Since the eigenvalues and eigenvectors are independent of c, they can be preprocessed and stored at negligible expense. Rather than building the inverse itself, a matrix-times-matrix operation can be avoided by multiplying, one at a time, the matrix pieces of (31) by the right-hand-side vector until the solution vector is attained. This results in a total operation count per time step of order $N_1 N_2 N_3 N_3$, large but tolerable.

Green's function solution of the normal velocity equation

One further detail must be mastered before we can march in time through the set of discrete equations. No Physical boundary conditions on ϕ (ϕ at the collocation points 0 and N_3) are available since ϕ is an intermediate variable used to split equation (3) into two parts. However, the Neumann condition of the normal velocity at the boundary can be used to constrain ϕ on the boundary as follows. The continuity equation on the boundaries is given by

$$0 = A_{ki} w_i^{n+1} + ik_1 u_k^{n+1} + ik_2 v_k^{n+1}, \tag{32}$$

where

$$i = 0 \text{ to } N_3,$$

$$k = 0 \text{ and } N_3.$$

Since the u and v velocities are known on the boundaries, (32) serves as a Neumann condition on w. We must pick ϕ on the boundaries so that (32) is satisfied. From (29), (30) and (32) we see that ϕ at 0 and N_3 affects (32) linearly. Therefore, this effect can be expressed by

$$0 = A_{ki} w_i^{n+1} + ik_1 u_k^{n+1} + ik_2 v_k^{n+1} = [G_{kj}]\{\phi_j^{n+1}\} + \{b_k\}, \tag{33}$$

where

$$G^{-1} \equiv \text{discrete Green's function},$$

$$b = b(u_k^{n+1}, v_k^{n+1}, w_i^{n+1}, \phi_{\text{RHS}}),$$

$$i = 0 \text{ to } N_3,$$

$$k = 0 \text{ and } N_3, \qquad j = 0 \text{ and } N_3.$$

The constant part, b, of this linear relationship is a function of the Dirichlet conditions on the velocity and ϕ_{RHS}. Inversion of the matrix yields the Green's function, G^{-1} (Kim *et al.*[7]). Thus, to solve the small linear system in (33), we must extract G and b, then invert B to solve for ϕ on the boundaries. Equation (34) shows how b is obtained. The divergence on the boundaries gives b, when ϕ on the boundaries is set to zero:

$$b_k = A_{ki} w_i^{n+1} + ik_1 u_k^{n+1} + ik_2 v_k^{n+1} \quad \text{using } \phi_j^{n+1} = 0, \tag{34}$$

where

$$i = 0 \text{ to } N_3,$$

$$k = 0 \text{ and } N_3, \qquad j = 0 \text{ and } N_3.$$

Equation (35) shows how G is extracted:

$$G_{kp}=A_{ki}w_i^{n+1}+ik_1u_k^{n+1}+ik_2v_k^{n+1}, \quad \text{with } \phi_j^{n+1}=\delta_{jp} \text{ and } u_k^{n+1}=v_k^{n+1}=w_i^{n+1}=\phi_{\text{RHS}}=0, \tag{35}$$

where

$$\delta_{jp} \equiv \text{unit Kronecker delta (real)},$$

$$i=0 \text{ to } N_3,$$

$$k, j, p=0 \text{ and } N_3.$$

To extract G, calculate the divergence on the boundary with the boundary values of u and v and with all values of w and ϕ_{RHS} set to zero. Then cycle a value of one (with the other zero) through the elements of ϕ on the boundary, which gives the columns of G. In obtaining G, we are setting b to zero and passing the identity matrix through the vector that multiplies G (ϕ on the boundary).

After G and b are extracted, G is inverted and multiplied by $-b$ to obtain ϕ on the boundary. Note that G is independent of any variables that change at each time step and can, therefore, be precalculated, inverted, and saved once for all time steps.

The foregoing process solves the fourth-order partial differential equation for w, (3), with the correct boundary conditions on w by solving two second-order equations twice, (29) and (30). Since the appropriate ϕ on the boundary must be determined for each wave-number pair, the storage requirement for G is on the order of N_1N_2, which is small. The extra computation expense is to make an extra pass through (29) and (30). Thus, for every time step we must solve five ODEs in the normal direction N_1N_2 times.

Discretization of the temperature equation

The discretization of the temperature field is easier than that of the velocity field. The temperature equation, (2), is first time split by the same technique used for the velocity field to give (36):

$$\left(1-\frac{\Delta t}{2Pe}\nabla^2\right)T^{n+1}=T_{\text{RHS}}, \tag{36}$$

where

$$T_{\text{RHS}}=\left(1+\frac{\Delta t}{2Pe}\nabla^2\right)T^n+\Delta t(\alpha H_T^n+\beta H_T^{n-1}),$$

$$H_T=\left(\frac{\partial T}{\partial x}u+\frac{\partial T}{\partial y}v+\frac{\partial T}{\partial z}w\right).$$

The constants α and β and the Runge–Kutta step size are the same as those of the velocity field. Note that we have treated the quasi-linear convective terms explicitly again since it is not computationally feasible to calculate a Jacobian. Equation (36) is then Fourier-transformed in the two homogeneous directions with the same DFTs used in the velocity field integration to give

$$\left[1-f_T\left(-k_1^2-k_2^2+\frac{\mathrm{d}^2}{\mathrm{d}z^2}\right)\right]T^{n+1}=T_{\text{RHS}}, \quad \text{with } T^{n+1} \text{ on } \partial D_z, \tag{37}$$

where

$$f_T=\frac{\Delta t}{2Pe}.$$

Note that, although the symbol did not change, the temperature variable in (37) is complex-valued and has been Fourier transformed in the two homogeneous directions, and it is assumed that the temperature field is periodic in those directions and has the same periodic lengths as the velocity field. The aspect ratio does not appear in the equation since it is built into the wave number. The evaluations of the convective terms containing T_{RHS} are completely de-aliased with the same technique used for the velocity field.

Discretization in the normal direction is done with the same collocation scheme used in the normal integration of the velocity field. The result is

$$[B_{ij}-c_T I_{ij}]\, T_j^{n+1} = -\frac{1}{f_T}(T_{\mathrm{RHS}})_i - B_{ik} T_k^{n+1}, \tag{38}$$

where

$$c_T = \left(\frac{1}{f_T} + k_1^2 + k_2^2\right),$$

$$i = 1 \text{ to } N_3 - 1 \quad \text{and} \quad j = 1 \text{ to } N_3 - 1,$$

$$k = 1 \text{ and } N_3.$$

The Dirichlet conditions on the temperature at the boundaries are applied by moving the known boundary information from the left to the right-hand side of (38), which is then in the same form as (28)–(30), so we can use (31) to solve the linear system, (38). This means that the eigenvectors and eigenvalues of B_{ij} can be preprocessed and stored and used to solve equation (38) for all of the wavenumber pairs to give about $N_1 N_2 N_3 N_3$ operations for each time step.

The total number of operations (ops) for one global step, or three Runge–Kutta substeps is given approximately by

$$\begin{aligned}\mathrm{ops} = 3\{&N_1 N_2 [7 N_3 N_3 + 12 N_3 \log_e(N_3)] + 13\, N_3 [N_1 (1{\cdot}5 N_2) \log_e (1{\cdot}5 N_2) \\ &+ N_2 (1{\cdot}5 N_1) \log_e (1{\cdot}5 N_1)]\}.\end{aligned} \tag{39}$$

The storage requirements for all of the variables is about $12\, N_1 N_2 N_3$.

3. CHOICE OF FLOW PARAMETERS AND GRID SIZE

The choice of Reynolds number was based partly on considerations of a particular project and partly of computational limitations. The value we choose was 180 based on channel half-width and friction velocity, which is the same as that used by Moser and Moin[6] and Kim *et al.*[7] with a grid a little larger than the size we considered practical for our resources. Those authors argued that a Reynolds number of 180 for smooth, infinite, parallel plates is the minimum for consistent, self-sustained turbulence, although Lyons *et al.*[8,9] obtained good results with a Reynolds number of 150. The Reynolds number of 180 is equivalent to a Reynolds number of 2800 based on bulk-average velocity and channel half-width or 11 200 based on bulk-average velocity and 4 times the hydraulic radius, which would be the Reynolds number in a round pipe that would yield a structurally similar flow near the wall.

The lengths over which the flow is periodic in the streamwise and spanwise directions is governed by the chosen aspect ratios (lengths relative to the channel depth). Since the turbulent structures are stretched in the flow direction, it is prudent to stretch the distance between grid points in the flow direction relative to that in the spanwise direction. Moser and Moin[6] recommend using aspect ratios such that the domain lengths scaled by the channel half-width are

4π, $4\pi/3$ and 2 for the streamwise, spanwise and normal directions, and we have chosen the same values. In terms of wall units, v/u_τ, these lengths are 2262^+, 753^+ and 360^+, where the plus sign refers to a distance non-dimensionalized by v/u_τ.

Kim *et al.*[7] used a grid of (128, 128, 65) points (wave numbers) in a simulation of channel flow that showed good agreement with experiment for first- and second-order statistics (mean velocity profile, intensities and Reynolds stress). They also used a grid of (192, 160, 129) points to achieve excellent agreement between their simulation and higher-order statistics such as skewness and flatness. We were unable to use a (128, 128, 65) grid because of storage limitations and used instead a grid of (96, 96, 65) points in spectral space to which 48 zeros were appended in the streamwise and spanwise directions to convert to (144, 144, 65) points in physical space. With this grid the spacing of the points was $15{\cdot}7^+$ in the streamwise direction and $5{\cdot}23^+$ in the spanwise direction, while in the normal direction the point nearest the wall was at $0{\cdot}21^+$, and the spacing at the pipe centre was 8·7.

4. INITIALIZATION

The computer time required to arrive at a stationary state depends on how far the initial estimates of the variables are from the final state. To conserve computer time, we were fortunate to obtain a fully developed turbulent velocity field from the Center for Turbulence Research at NASA Ames Research Center. The Reynolds number was the same as the one we used but their velocity field used (128, 128, 129) wave numbers. Their computation had been run for 250 h on a Cray X-MP/48 after being initialized with the output from a large eddy model. We interpolated this field onto our grid by changing the larger field to spectral space, truncating the global series to the desired length, and transforming back. Although the velocity field was at a stationary state in the NASA model, it had to come to a new stationary state under our model and grid size. We monitored the approach to the new state by calculating several statistics. After about 75 h on the Cray X-MP using one processor, the non-dimensional time reached a value of 4.0, which corresponds to about 4200 time steps, and we concluded that our field was effectively at its final state. Details can be found in Rutledge.[16]

The temperature field was initialized by starting with a profile in the normal direction set to zero for all wave-number pairs except for the zero–zero mode. For this mode the Fourier wave number in both homogeneous directions is zero, and it is a profile in the normal direction obtained from an ensemble average on the temperature field in both homogeneous directions. We obtained an approximation to the average temperature profile in the normal direction by splicing together pieces of eddy-diffusivity models in such a way that the entire profile was infinitely differentiable to machine precision. (The spectral technique for integrating the temperature equation requires that the temperature field be initialized with functions that are at least 64th-order continuous in the normal direction.)

5. THE DECAY OF THE FOURIER AND CHEBYSHEV COEFFICIENTS

The quality of the spatial numerical solution can be judged from the decay of the coefficients of the approximating series. For an accurate simulation, the Fourier and Chebyshev coefficients should decay rapidly enough with term number so that the last few terms of the series contribute negligibly to the sum. The coefficients are displayed in Figures 2–4 in the form of energy spectra. The streamwise energy spectra, for example, are functions of the streamwise wave number, k_1,

and the normal direction and are defined in (40); analogous definitions hold for other spectra:

$$E_1(u_iu_i)(k_1, z)=\frac{1}{2N_2}\sum_{i_2=0}^{N_2-1}[u_i(k_1, y_{i2}, z)u_i(k_1, y_{i2}, z)+u_i^*(k_1, y_{i2}, z)u_i^*(k_1, y_{i2}, z)], \quad (40)$$

where $E_1(u_iu_i)$ is the streamwise spectral energy for the velocity in the ith direction, u_i is the ith direction velocity Fourier-transformed only in the streamwise direction, k_1 is the streamwise wave number, and u_i^* is the complex conjugate of u_i.

The spectra decay most rapidly near the channel centre, and so in Figures 2–4 we show the nine 'worst-case' spectra, which occur near the wall; data are shown at $z^+ = 5{\cdot}39$. The E_1 spectra are

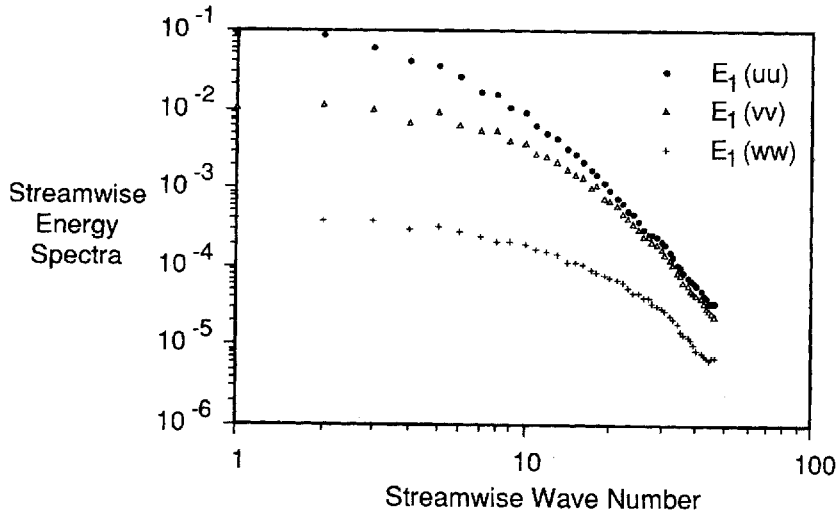

Figure 2. Spectra of streamwise Fourier coefficients at $z^+ = 5{\cdot}39$

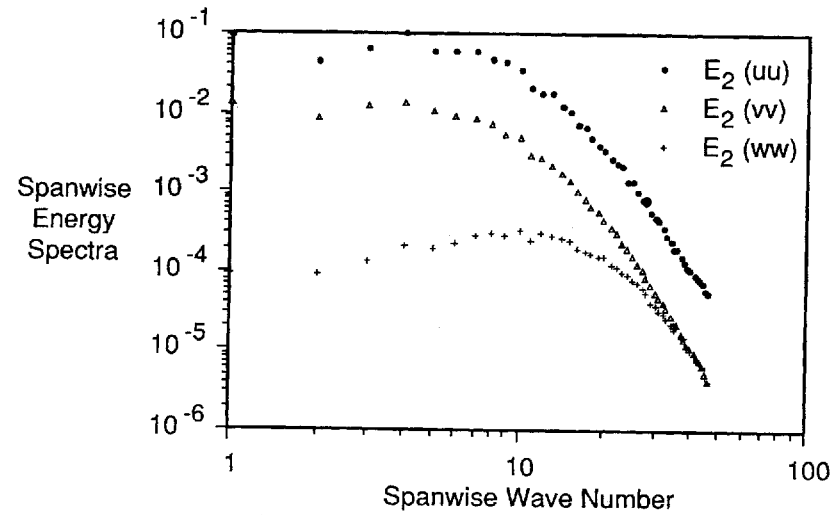

Figure 3. Spectra of spanwise Fourier coefficients $z^+ = 5{\cdot}39$

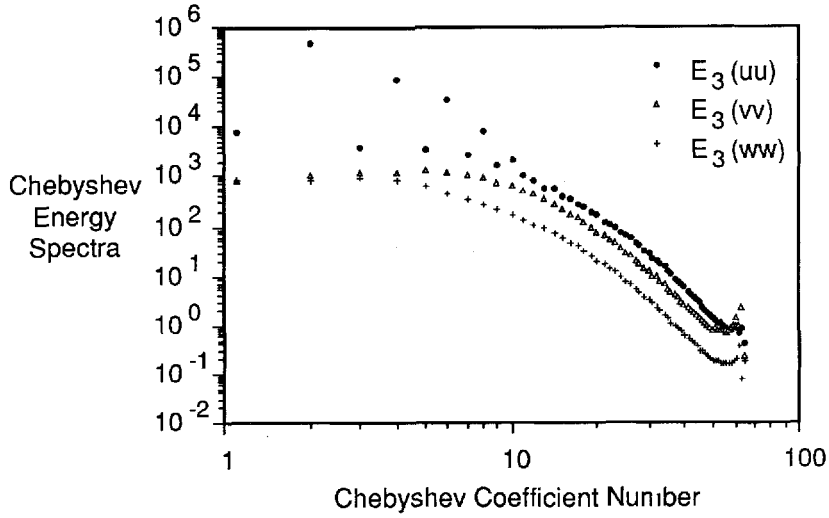

Figure 4. Spectra of Chebyshev coefficients

averaged in the spanwise direction and over six time samples within one non-dimensional time unit. Similarly, the E_2 spectra are averaged over time and the streamwise direction. Of these spectra, the worst case is $E_1(ww)$, which decays by a factor of about 60. All other spectra decay by more than two orders of magnitude. An upturn at the highest wave numbers is referred to as a wavenumber pile up and can be a sign that the length of the series is too short. There is a slight upturn in $E_1(ww)$, but it is probably not damaging.

The spectra of the Chebyshev series, shown in Figure 4, are defined by

$$E_3(u_iu_i)(n)=\frac{1}{N_1N_2}\sum_{i_1=0}^{N_1-1}\sum_{i_2=0}^{N_2-1}c_i(x_{i1},y_{i2},n)\,c_i(x_{i1},y_{i2},n), \tag{41}$$

where

$E_3(u_iu_i)$ = Chebyshev spectral energy for the ith velocity direction,

$$c_i(x_{i1},y_{i2},n)=\sum_{i_3=0}^{N_3}U_i(x_{i1},y_{i2},z_{i3})T_n(z_{i3}),$$

T_n = nth-order Chebyshev polynomial.

The rate of decay of the Chebyshev series is superior to that of the Fourier series even though fewer terms are used (64 vs. 96). Even though there is a slight upturn at the high-term numbers, the ratio of highest to the lowest term exceed three orders of magnitude even in the worst case. Presumably, with more terms the upturn would disappear, but we believe the effect on the velocity field would be negligible.

6. STATISTICS OF THE VELOCITY FIELD AT STATIONARY STATE

Presented here are several comparisons between experimental data and data statistically reduced from our simulations. The simulated data are averaged over all spatial points in the homogeneous directions and five places in time between 5·175 and 5·215 non-dimensional time units.

We have not included a figure of the average streamwise velocity profile because the calculations are in almost perfect agreement with the calculations of Kim *et al.*[7] (hereafter refered to as KMM). They are also in satisfactory agreement with the experimental data of Eckelmann[28] for his Reynolds numbers $[(u_\tau\delta/\nu]$ of 143 and 210, which bracket our value of 180, provided those data are rescaled by increasing Eckelmann's value of u_τ by 6% for reasons noted by KMM. Eckelmann's data were taken across the width of a channel at a position close to the spanwise centre of the channel, which had an effective aspect ratio of about 7. (The actual aspect ratio was 3·9, but the upper surface, which was normal to the spanwise direction, was free and affected the flow more like a channel centre than a wall.) Hence, his data would be a good match to the data in a channel of infinite aspect ratio. It should be noted that $y^+ = 36$ occurs at $y/\delta = 0{\cdot}2$. Thus, since the law of the wall is inaccurate for $y/\delta > 0{\cdot}2$, while the velocity defect law is not valid for $y^+ < \sim 36$, there is no region where the two laws overlap and, therefore, there should be no significant range in which the logarithmic mean velocity profile is expected;[27] the Reynolds number is too low for the existence of a significant logarithmic region.

Figures 5 and 6 compare spanwise and normal near-wall turbulence intensities defined by $u_i' = (\overline{u_i^2})^{1/2}$ with the calculations of KMM and of Lyons *et al.*[8] (hereafter refered to as LHM), and experimental data of Eckelmann[28] and Kreplin and Eckelmann.[29] The agreement among all studies for the streamwise intensity is quite good and so are not shown. There is less agreement, however, in the spanwise and normal directions. Our normal intensities fall significantly below those of Eckelmann[28] and Kreplin and Eckelmann[29] but are in good agreement with the calculations of KMM and LHM. The calculations of LHM were shown in their paper to be in near perfect agreement with the data of Niederschulte.[30] (Calculations for $z^+ > 40$ are not shown since the proper scaling is intensity vs. z/δ and would require another figure.)

The spanwise intensity is the most interesting. Our calculations fall well below the data of Eckelmann in the range $4 < z^+ < 15$, although, outside that range, they are in good agreement. They also fall a little above the calculations of LHM, made with four grids of increasing size, the largest being (128, 128, 65) in physical space. They concluded that the solutions of the spanwise

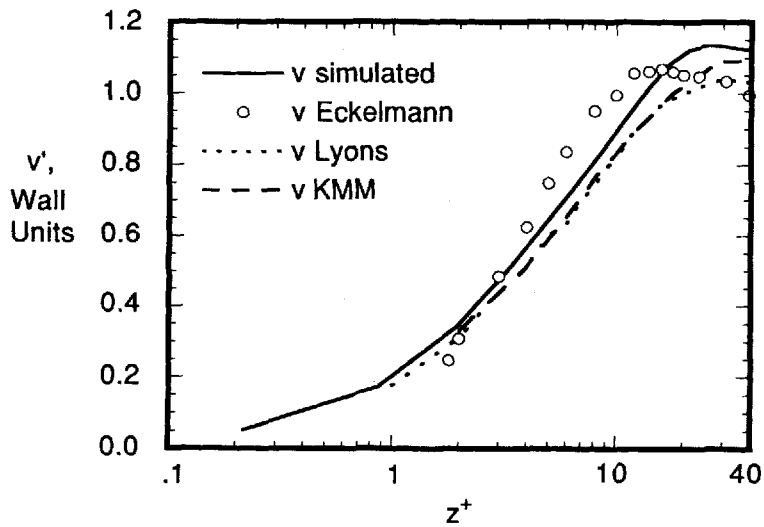

Figure 5. Spanwise turbulence intensity profile

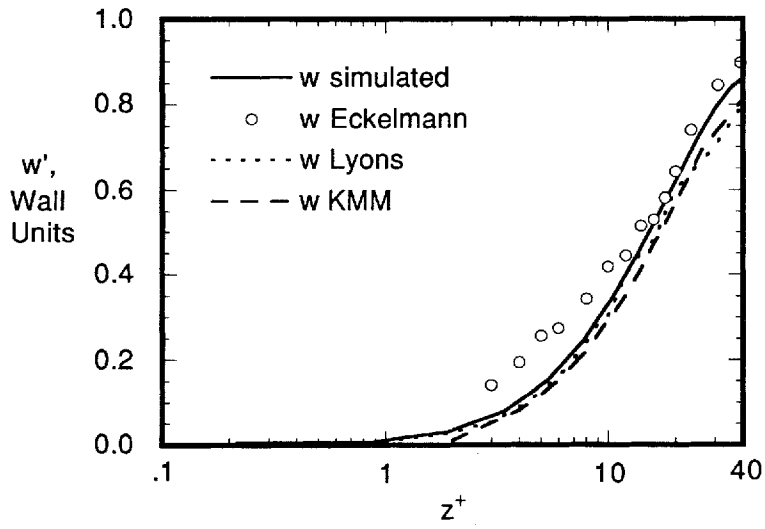

Figure 6. Normal turbulence intensity profile

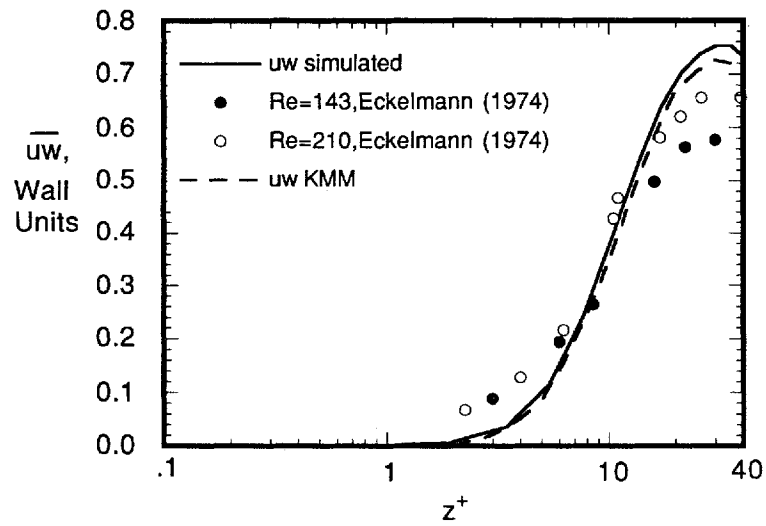

Figure 7. Reynolds stress profile

intensity had not coverged as a function of grid resolution. Our data with a grid of (144, 144, 65) support that conjecture.

Figure 7 shows the *uw* Reynolds stress in the wall region together with Eckelmann's data at Reynolds number of both 143 and 210. The agreement with KMM is good all the way to the channel centre, but there is some disagreement with the data of Eckelmann, as shown.

Calculations for the steamwise skewness, $\overline{u_i^3}/(u_i)^3$, and streamwise flatness, $\overline{u_i^4}/(u_i')^4$ agree well with the data of Eckelmann[28] and Barlow and Johnston[31] and the calculations of KMM and

LHM and so are not shown. Figure 8 compares our calculations of normal skewness to other data. In the region $z^+ < 40$ our calculations agree well with those of KMM but differ somewhat from the others. For $z^+ > 40$ the agreement among all of the data is good. As noted by KMM, the skewness for the spanwise velocity, v, should be zero whereas ours has non-zero but small values.

Our calculations of normal flatness agree well with those of KMM and LHM throughout the range $z^+ > 2$. It is disturbing, however, that all three calculations disagree significantly with the carefully obtained data of Kreplin and Eckelmann[29] and Barlow and Johnston[31] in the region $2 < z^+ < 10$, as noted in Figure 9.

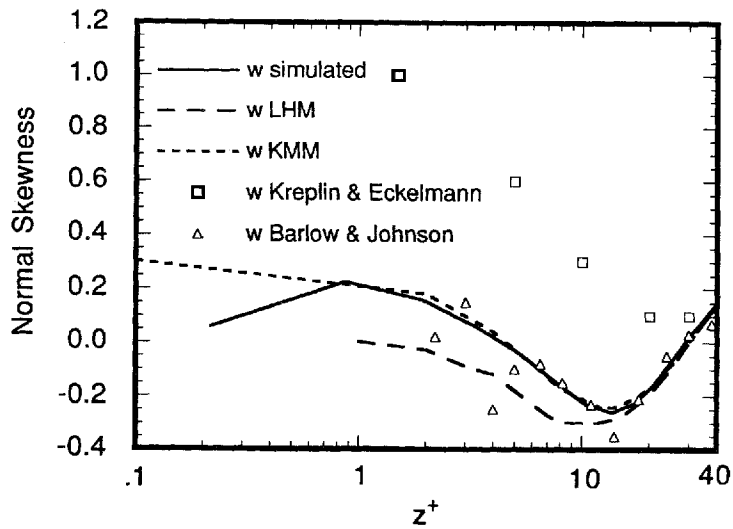

Figure 8. Normal skewness profile near the wall

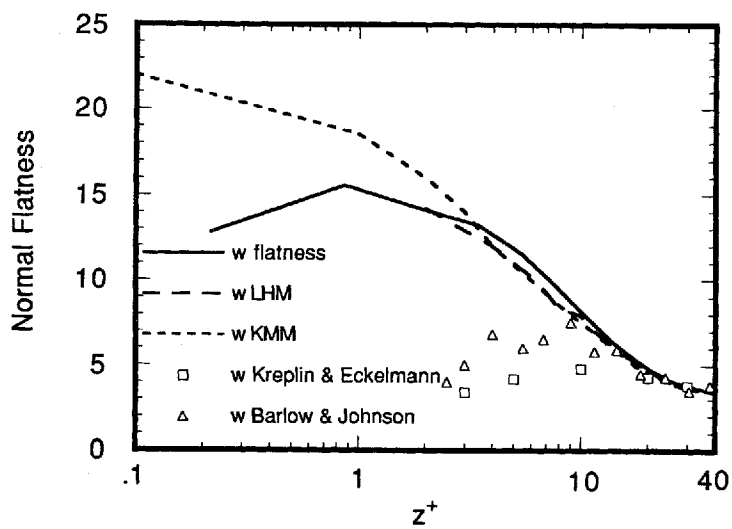

Figure 9. Normal flatness profile near the wall

The foregoing comparisons provide evidence that our Navier–Stokes solver is indeed simulating turbulent flow in a channel. While the extent of the calculations is not as complete as was done by KMM, we believe that it is adequate for our purposes and is the best possible with the resources available.

7. TWO-POINT CORRELATIONS

Two-point correlations are important because they can provide insight into the structures present in the flow, and they are a severe test of a turbulent flow calculation. Two-point correlations are the time or spatially averaged products of two dependent variables separated by a spatial vector. The streamwise two-point correlation for the streamwise velocity is defined in (42), and is a function of the separation vector of the points, which for this correlation lies on the x-axis, and the location in the normal direction, z.

$$R_1(uu)(\xi, z) = \left\{ \frac{\overline{u(x+\xi, y, z, t)\, u(x, y, z, t)}}{\overline{u'(x, y, z, t)\, u'(x, y, z, t)}} \right\}, \tag{42}$$

where

$R_1(uu)$ = streamwise two-point correlation for streamwise velocity,

u = fluctuating part of the streamwise velocity,

ξ = streamwise separation between points,

$\bar{}$ = average in streamwise and spanwise directions and time.

Similar correlations may be defined for other combinations of velocity components, temperature, or velocity and temperature, and for other directions of the spatial vector between the points. The correlations are generally normalized by the root-mean-square values of the two dependent variables, i.e. the correlations equal one for zero separation of the points. All of our

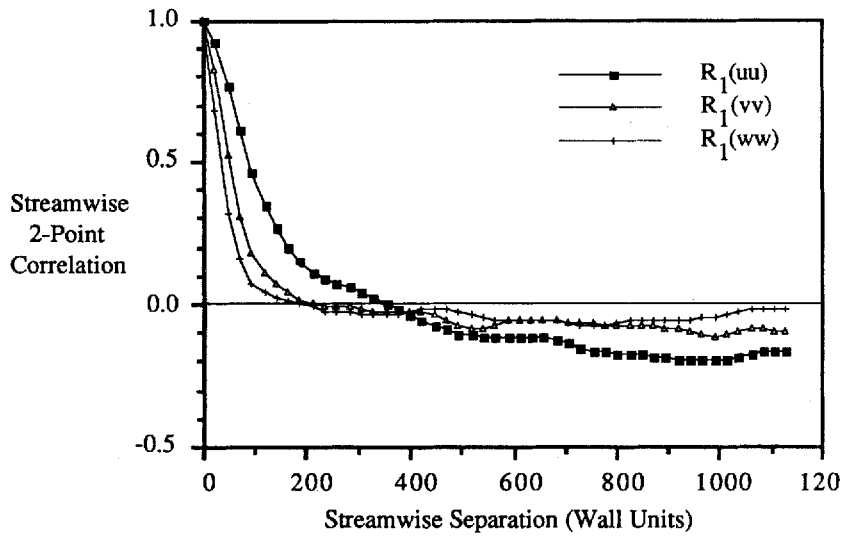

Figure 10. Streamwise two-point correlations at $z^+ = 5{\cdot}39$

correlations were averaged over six samples in time from 4·27 to 5·215 time units and twelve samples in the homogeneous directions in space.

Figures 10 and 11 show the three streamwise and spanwise correlations close to the wall at $z^+ = 5{\cdot}39$. The minima of the spanwise correlations, $R_2(uu)$ at $z^+ \approx 50$, $R_2(vv)$ at $z^+ \approx 60$ and $R_2(ww)$ at $z^+ \approx 25$ agree well with position and amplitude of the R_2 correlations of KMM, who noted that the minimum in $R_2(uu)$ gives an estimate of the mean separation between high- and low-speed fluid. Thus, the mean spacing between wall streaks would be about 100 wall units, which is consistent with the spacing shown later in Figure 19. Our curves of $R_2(uu)$ and $R_2(vv)$

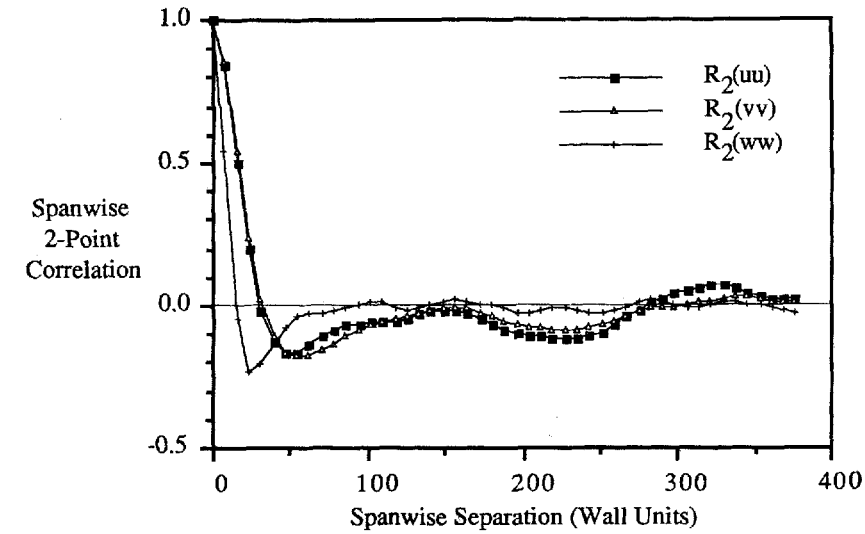

Figure 11. Spanwise two-point correlations at $z^+ = 5{\cdot}39$

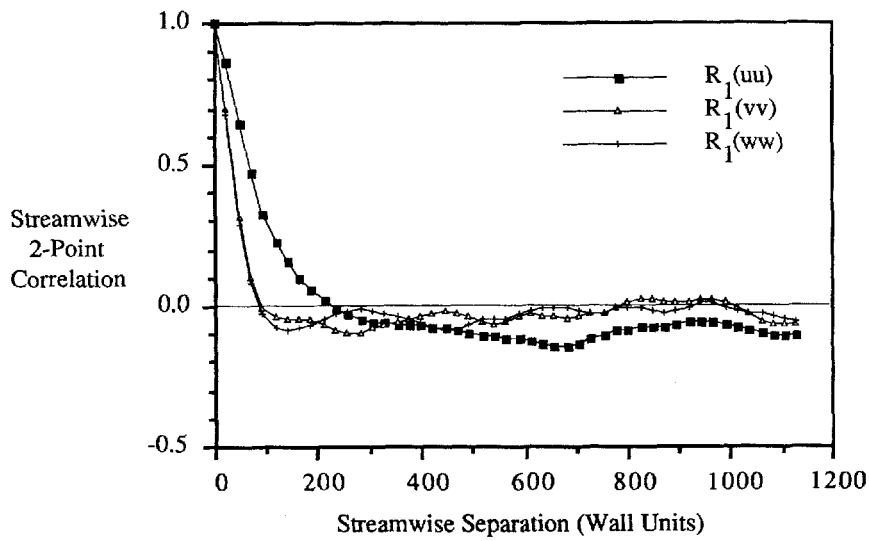

Figure 12. Streamwise two-point correlations at $z^+ = 144{\cdot}8$

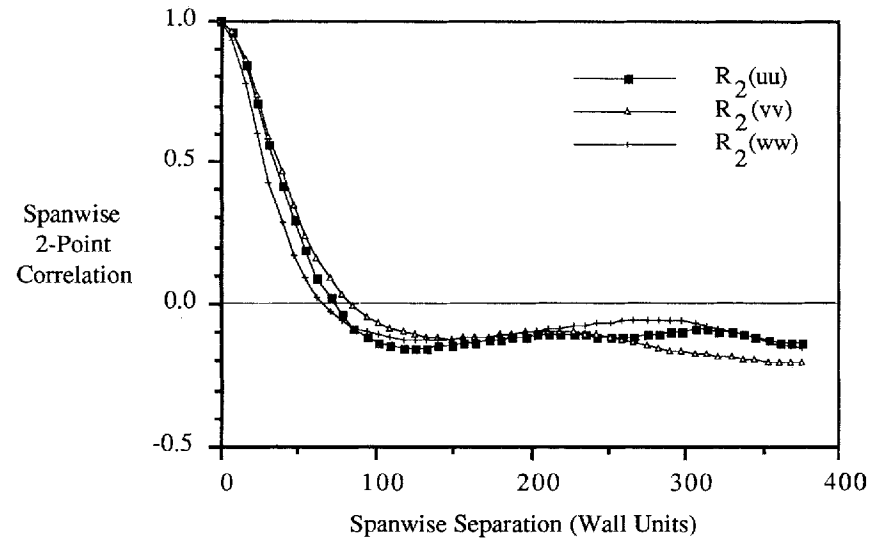

Figure 13. Spanwise two-point correlation at $z^+ = 144{\cdot}8$

show a second minimum at about $z^+ \approx 220$ or $z/\delta \approx 1{\cdot}2$, which do not appear in the R_2 spectra of KMM.

Figures 12 and 13 show the streamwise and spanwise correlations near the channel centre at $z^+ = 144{\cdot}8$. These correlations as well as those in Figure 10 do not decay to a satisfactorily low value over half of the periodic domain, as they should, although the deviations from zero are small. The reasons for this are not certain. Presumably, the decay would be improved with longer periodic lengths or more Fourier modes or more samples in the averages. The correlations of KMM are better, and they used the same periodic length but more modes and sampled over about ten times as many samples.

8. THE TEMPERATURE FIELD

Our original intention was to calculate the temperature field for a fluid with a Prandtl number 7. However, after computing for 0·65 time units, the time rate of change of several statistical measures of the temperature field was still unacceptably large and was decreasing only slowly. Therefore, rather than pursue a probable waste of computational resources, the Prandtl number was changed to 4. This change helped, but the rate of change was still very small. Moreover, a plot of the $E_3(TT)$ spectrum of the temperature field Chebyshev coefficients after 3·08 time units showed a decay of a ratio of the coefficients of only 25 and a significant upturn for the highest coefficients. Finally, therefore, we changed the Prandtl number to 0·72, the approximate value for air at room temperature. After computing for 5 time units, the rates of change of all terms in the averaged energy equation were very small, and we concluded that the temperature field had reached a stationary state.

An indication of the suitability of our spatial approximations is the decay of the spectra of the temperature Fourier and Chebyshev coefficients, $E_1(TT)$, $E_2(TT)$ and $E_3(TT)$, in a manner similar to that done for the velocity field. The results were slightly better than those for the velocity field, and the smallest ratio of high to low coefficients in one spectra was about 180.

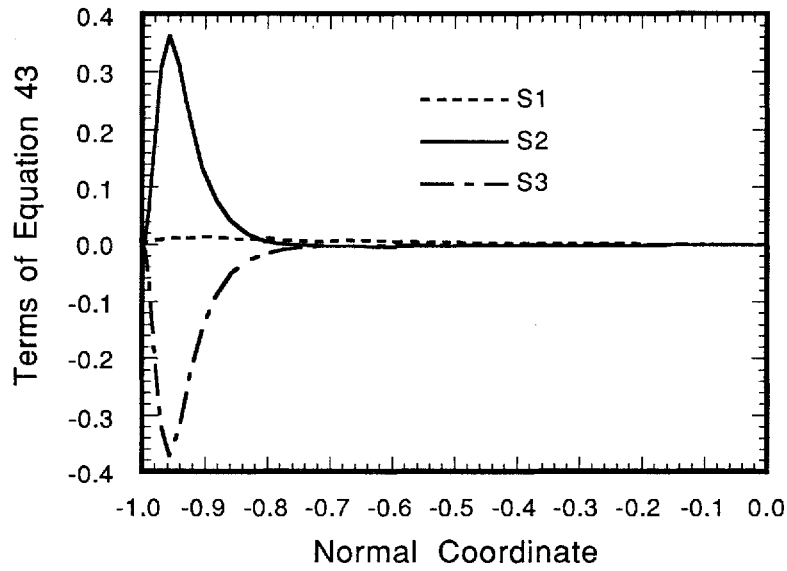

Figure 14. Terms of equation (43)

The time-averaged equation for the transport of $\bar{T}^2/2$, the thermal equivalent of the mean kinetic energy of the velocity, can be written

$$0 = S_1 + S_2 + S_3, \tag{43}$$

where

$$S_1 = \frac{1}{2}\frac{\partial}{\partial t}\bar{T}^2,$$

$$S_2 = \bar{T}\frac{\partial}{\partial z}\overline{\theta w},$$

$$S_3 = -\frac{1}{Pe}\bar{T}\frac{\partial^2 \bar{T}}{\partial z^2}$$

and Figure 14 shows a plot of the three terms as functions of the normal co-ordinate, averaged in both homogeneous directions. The profile of S_1 is close to zero for the entire span, indicating that a stationary state had been achieved. The other two terms represent turbulent and molecular diffusion in the normal direction. The profiles show that the average and fluctuating temperature fields interact significantly with each other only in a boundary layer about 20% of the channel half-width or about 35 wall units.

The temperature and heat flux profiles averaged over the homogeneous directions at 5·215 time units are shown in Figure 15. The scale for the heat flux is expanded. The heat flux should, of course, be constant. The fact that it deviates about 13% from its average value suggests either that the temperature field is not at a true stationary state or that averaging over time as well as space is needed. However, we were unable to carry out computations further in time.

Figure 16 shows the profile of the mean-square temperature fluctuation, $(\overline{\theta^2})$.

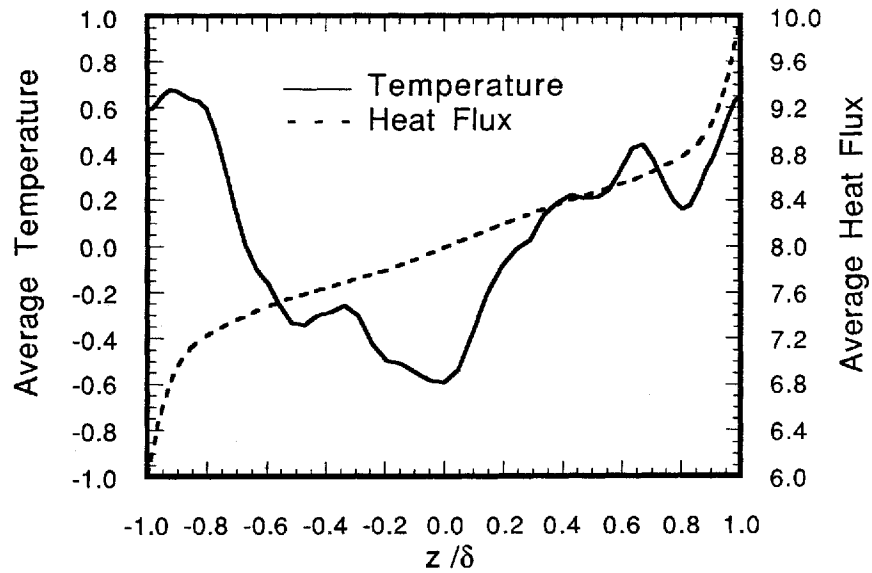

Figure 15. Temperature and heat flux profiles

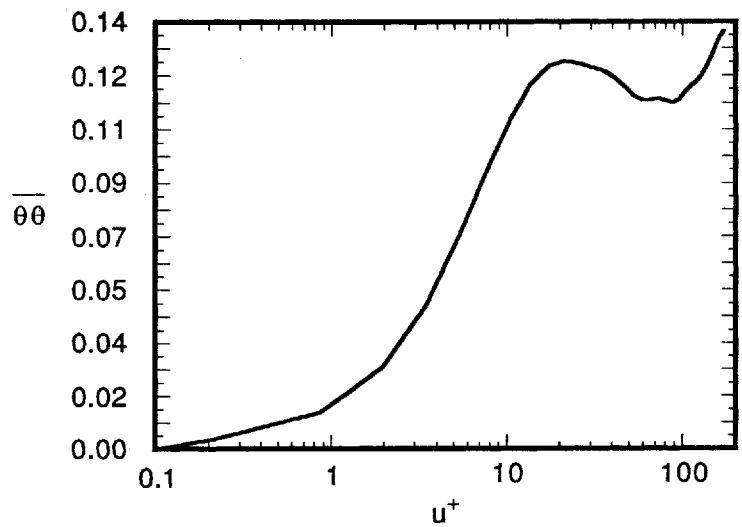

Figure 16. Mean-square temperature fluctuation profile

Functions of practical interest are the eddy viscosity and eddy diffusivity, defined in dimensional units by

$$\tau/\rho=(\nu+\nu_t)(\partial U/\partial z) \quad \text{or} \quad -\overline{uv}=\nu_t(\partial U/\partial z) \tag{44}$$

and

$$q/\rho C_p=-(\alpha+\alpha_t)(\partial T/\partial z)=-\alpha(1+Pr\alpha_t/\nu)(\partial T/\partial z) \quad \text{or} \quad -\overline{v\theta}=\alpha_t(\partial T/\partial z), \tag{45}$$

where ν_t and α_t are the eddy or turbulent kinematic viscosity and eddy thermal diffusivity.

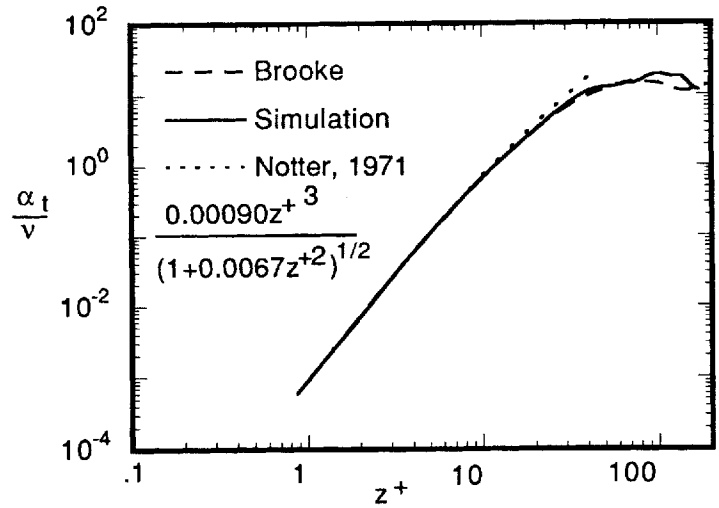

Figure 17. Eddy-diffusivity profile

Figure 17 shows the simulated eddy diffusivity in the wall region together with calculations of Brooke and Hanratty[32] and the empirical expression of Notter and Sleicher[33] for $z^+ < 45$. Of special interest is the slope and position of the line in the limit as $z^+ \to 0$. As unlikely as it sounds, our calculations agree to two significant figures with the empirical equation in this limit; i.e. $\alpha_t/\nu = 0{\cdot}00090\ z^{+3}$. This disagrees with the value of $\alpha_t/\nu = 0{\cdot}000775\ z^{+3}$ found by LHM. However, Prof. Hanratty (see Reference 32) supplied the authors with revised calculations of α_t/ν, and the results are shown by the line labeled 'Brooke'. Apparently, the limiting behaviour of this line is given approximately by $\alpha_t/\nu = 0{\cdot}00087\ z^{+3}$. The small difference cannot be seen on the figure. In any case, the behaviour of α_t/ν is of practical importance in the calculation of heat transfer by eddy diffusivity models.

9. FLOW VISUALIZATION

From laboratory observations of smoke or fog one can speculate about structures in the velocity field. Similarly, we can use temperature contour plots to get some idea of the structures that are present in the velocity field. The temperature field also experiences conduction, which complicates interpretation.

The top third of Figure 18 shows a streamwise–normal contour plot of the temperature field at a fixed value of y and at 4·895 non-dimensional time units. A profile of the streamwise average velocity has been placed at the same vertical position for reference. Note that all distances are in wall units and that the scale has been expanded by a factor of 2 in the normal direction. In the figure, a box has been placed around a structure of interest. The central and bottom thirds of the figure show temperature fields similar to the top third but at times 4·935 and 4·975. During each of the 0·04 time intervals between the plots, fluid having bulk average velocity would have moved 112 wall units, Undistorted boxes have been placed on the plots at intervals of 112 wall units so as to follow an element of fluid ejected downward. At the top this ejection is seen to increase the thickness of the warm layer near the wall. In the central plot the ejected fluid further undermines the layer near the wall, and in the bottom subfigure the ejection has been further convected

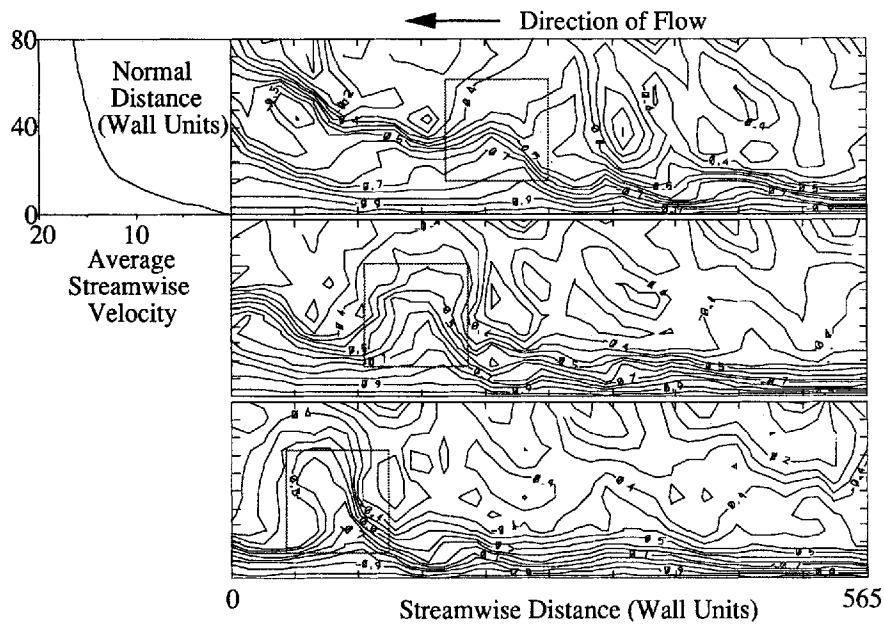

Figure 18. Streamwise–normal-temperature contours following the flow

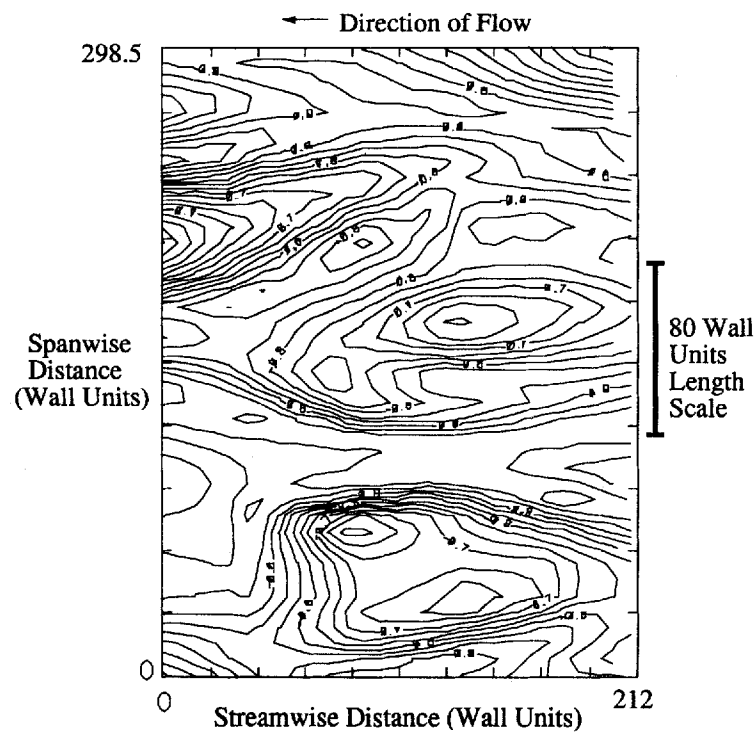

Figure 19. Temperature contours at $z^+ = 5{\cdot}39$

downstream, and the velocity profile has tilted the top of the structure to the left. Events such as this obviously augment the heat transfer rate. The interested reader might compare these plots with photographs of flow visualization in a turbulent boundary layer in the book by Van Dyke[34] (Figure 160 due to Falco[35]) recalling that the figures here must be compressed by a factor of two in the spanwise direction.

In a similar manner, we have plotted contours of the temperature field with the spanwise and normal directions as the abscissa and ordinate, respectively. One such plot, for example, was at $x^+ = 0$ and at a time of 5·025. Another plot was then made at a time of 5·049, at which time the fluid of bulk average velocity would have been swept to $x^+ = 70{\cdot}7$, the location of the plot. A third plot was at a time of 5·073 and at $x^+ = 141{\cdot}4$. In this way, structures were identified and followed. From such observations we infer that the time required for the break-up of fluid structures is typically about 0·16 non-dimensional time units or about 30 time units based on wall shear stress and kinematic viscosity, which agrees with that observed by Falco.[35]

Finally, we present a contour plot of the temperature field at a plane parallel to the boundary. Figure 19 is at 5·39 wall units above the solid surface. Cantwell[36] concludes that the length scale of the structures, the distance between streaks, at this level is about 80 wall units, and there is a marker beside the plot that shows this length. Although there are only a few structures present, 80 appears to be a reasonable length scale. Again, it is instructive to compare these plots with the photograph of the sublayer structure at 9–14 wall units shown by Van Dyke.[34]

The plots shown here are but a small sample of the many hundreds that could be made of our temperature field. They illustrate, however, the potential power of simulation to reveal information about structures in turbulent flow.

10. CONCLUSIONS

A computer program has been developed that successfully models the major characteristics of turbulent flow and heat transfer in a two-dimensional channel at low Reynolds numbers. The program uses no approximations aside from periodic domains in the streamwise and spanwise directions, a finite number of Fourier modes in those directions, and a finite number of Chebyshev polynomials in the normal direction. The program lays the foundation for the investigation of heat transfer with wavy boundaries, which forms Part II of this study.

ACKNOWLEDGEMENTS

We gratefully acknowledge the support of Argonne National Laboratory and fellowship support from the Amoco Foundation. Most of the computer time for this research was provided by the National Center for Supercomputer Applications (NCSA), and some computer time and excellent support was also provided by the San Diego Supercomputer Center (SDSC). Appreciation is also extended to Drs. Bruce A. Finlayson and James J. Riley of the University of Washington and Dr. Robert Moser of NASA Ames Research Center for their valuable technical input. We also thank the Center for Turbulence Research at the NASA Ames Research Center for providing the fully developed velocity field used to initialize our calculations. Finally, we thank the Department of Chemical Engineering at the University of Guadalajara for providing the time and resources for the preparation of the manuscript.

REFERENCES

1. J. H. Fergizer, 'Simulation of incompressible flows', *J. Comput Phys.*, **69,** 1–48 (1987).
2. S. A. Orszag and G. S. Peterson, 'Numerical simulation of three-dimensional homogeneous isotropic turbulence', *Phys. Rev. Lett.*, **28(2),** 76–79 (1972).
3. S. A. Orszag and L. C. Kells, 'Transition to turbulence in plane Poiseuille and plane Couette flow', *J. Fluid Mech.*, **96,** 159–205 (1980).
4. P. Moin and J. Kim, 'The structure of the vorticity field in the turbulent channel flow. Part 1. Analysis of instantaneous fields and statistical correlations', *J. Fluid Mech.*, **155,** 441–464 (1980).
5. P. Moin and J. Kim, 'On the numerical solution of time-dependent viscous incompressible fluid flows involving solid boundaries', *J. Comput. Phys.*, **35,** 381–392 (1980).
6. R. D. Moser and P. Moin, 'Direct numerical simulation of curved channel flow', *NASA TM 85974*, 1984.
7. J. Kim, P. Moin and R. Moser, 'Turbulence statistics in fully developed channel flow at low Reynolds number', *J. Fluid Mech.*, **177,** 133–166 (1987).
8. S. L. Lyons, T. J. Hanratty and J. B. McLaughlin, 'Large-scale computer simulation of fully developed turbulent channel flow with heat transfer', *Int. j. numer. methods fluids*, **13,** 999–1028 (1991).
9. S. L. Lyons, T. J. Hanratty and J. B. McLaughlin, 'Direct numerical simulation of passive heat transfer in a turbulent channel flow', *Int. J. Heat Mass Transfer*, **34,** 1149–1161 (1991).
10. S. A. Orszag, 'Numerical simulation of incompressible flows within simple boundaries. I Galerkin (spectral) representations', *Stud. Appl. Math.*, **50,** 293–327 (1971).
11. A. J. Chorin, 'A numerical method for solving incompressible viscous flow problems, *J. Comput. Phys.*, **2,** 12–26 (1967).
12. A. Leonard and A. Wray, 'A new numerical method for the simulation of three-dimensional flow in a pipe', *NASA TM 84267*, 1982.
13. J. Kim and P. Moin, 'Application of a fractional-step method to incompressible Navier–Stokes equations', *J. Comput Phys.*, **59,** 308–323 (1985).
14. S. Abdallah, 'Numerical Solutions for the pressure poisson equation with Neumann boundary conditions using a non-staggered grid. I', *J. Comput. Phys.*, **70,** 182–192 (1987).
15. C. H. Ku, R. S. Hirsh and T. D. Taylor, 'A pseudospectral method for solution of the three-dimensional Navier–Stokes equations', *J. Comput Phys.* **70,** 439–462 (1987).
16. J. Rutledge, 'Direct simulation of enhancement of turbulent heat transfer by micro-riblets', *Ph.D. Dissertation*, University of Washington,. Seattle, 1989.
17. A. Wray and M. Y. Hussaini, 'Numerical experiments in boundary layer stability,' *Proc. Roy. Soc. Lond.*, **A392,** 373–389 (1984).
18. P. R. Spalart, 'Hybrid RKW3+Crank Nicholson', NASA Langley manuscript (no date).
19. C. Temperton, 'Self-sorting mixed radix fast fourier transforms', *J. Comput Phys.*, **52,** 1–23 (1983).
20. C. Temperton, 'Fast mixed radius real Fourier transforms', *J. Comput. Phys.*, **52,** 340–350 (1983).
21. C. Temperton, 'Implementation of a self-sorting in-place prime factor FFT algorithm, *J. Comput Phys.*, **58,** 283–299 (1985).
22. R. N. Bracewell, *The Fast Fourier Transform and Its Applications*, McGraw-Hill, New York, 1978.
23. G. F. Fox and S. A. Orszag, 'Pseudospectral approximation to two-dimensional turbulence', *J. Comput Phys.*, **11,** 612–619 (1973).
24. C. Lanczos, *Applied Analysis*, Prentice Hall, Englewood Cliffs, NJ, 1956.
25. P. Moin and J. Kim, 'On the numerical solution of time-dependent viscous incompressible fluid flows involving solid boundaries', *J. Comput Phys.* **35,** 381–392 (1980).
26. D. Gottlieb and S. A. Orszag, 'Numerical analysis of spectral methods: theory and applications', in *CDMS-NSF Mongraph 26*, SIAM, Philadelphia, 1977.
27. H. Tennekes and J. L. Lumley, *A First Course in Turbulence*, MIT Press, Cambridge, 1972, pp. 150–156.
28. H. Eckelmann, The structure of the viscous sublayer and the adjacent wall region in a turbulent channel flow', *J. Fluid Mech.*, **65,** 439–459 (1974).
29. H. Kreplin and H. Eckelmann, 'Behavior of the three fluctuating velocity components in the wall region of a turbulent channel flow', *Phys. Fluids*, **22,** 1233–1239 (1979).
30. M. A. Niederschulte, 'Turbulent flow through a rectangular channel', *Ph.D. Dissertation*, University of Illinois, Urbana, 1988.
31. R. S. Barlow and J. P. Johnson, 'Structure of turbulent boundary layers on a concave surface', *Report No. MD-47*, Dept. of Mech. Eng., Stanford University, Stanford, 1985.
32. J. Brooke and T. J. Hanratty, personal communication, 1992.
33. R. N. Notter and C. A. Sleicher, 'The eddy diffusivity in the turbulent boundary layer near a wall', *Chem. Eng. Sci.*, **26,** 161–171 (1971).
34. M. Van Dyke, *An Album of Fluid Motion*, The Parabolic Press, Stanford, 1982.
35. R. Falco, 'The probing of turbulence near a wall', *AIAA 13th Fluid and Plasma Dynamics Conference*, Snowmass, CO, 1980. AIAA-80-1356 Microfische.
36. B. J. Cantwell, 'Organized motion in turbulent flow', *Ann. Rev. Fluid Mech.*, **13,** 457–515 (1981).